Manganese (II) oxide-embedded dopamine-derived carbon nanospheres for durable zinc-ion batteries

Zixiang Zhou, Jianbo Tong*, Jiale Guo, Shuhan Liu, Shaofeng Guo, Zhipeng Qin, Zelei Chang, Chao Wang, Shuling Liu*

Department of Chemistry and Chemical Engineering, Shaanxi Collaborative Innovation Center of Industrial Auxiliary Chemistry & Technology, Key Laboratory of Auxiliary Chemistry and Technology for Chemical Industry, Ministry of Education, Shaanxi University of Science and Technology, Xi'an, Shaanxi 710021, China

*Corresponding author.

E-mail address: liushuling@sust.edu.cn

jianbotong@aliyun.com

Chemicals

The following reagents were used without further purifications. Manganese(III) acetate dihydrate ($Mn(CH_3COO)_3 \cdot 2H_2O$, AR, 97.0%), dopamine hydrochloride ($C_8H_{11}NO_2 \cdot HCl$, AR, 99%), tris(hydroxymethyl)aminomethane($C_4H_{11}NO_3$, AR, 99%), manganese sulfate tetrahydrate ($MnSO_4 \cdot 4H_2O$, AR, 98.0%), zinc sulfate heptahydrate ($ZnSO_4 \cdot 7H_2O$, AR, 98.0%), and doubly distilled water.

Material characterizations

Crystallographic phases of the samples are assessed using X-ray diffraction (XRD) employing a Bruker D8 Advance instrument in Bragg-Brentano geometry with a Cu target (λ = 0.154 nm). Thermogravimetric analysis (TGA) is conducted to analyze the degradation pattern of precursor samples (post-drying) from room temperature to 600 °C at a heating rate of 5 °C min^{-1} under N_2 flow, utilizing a thermogravimetric analyzer (STA7200RV, Hitachi). X-ray photoelectron spectroscopy (XPS) measurements are performed using an AXIS SUPRA instrument (Renishaw-invia). Field emission scanning electron microscopy (FE-SEM) at an accelerating voltage of 10 kV is employed to observe sample morphologies. Raman spectroscopy measurements are conducted using a Renishaw Invia Raman spectroscope. Transmission electron microscopy (TEM) equipped with energy-dispersive X-ray spectroscopy (EDS) (Xplore-30, Oxford), High-resolution transmission electron microscopy (HR-TEM), and selected area electron diffraction (SAED) patterns are obtained utilizing the FEI Tecnai G2 F20 instrument with an acceleration voltage of 200 kV.

Electrochemical characterizations

The cathode of the ZIBs is fabricated using active material, acetylene black as the conductive agent, and polyvinylidene fluoride as the binder (with a weight ratio of 7:2:1), and N-methyl-2-pyrrolidone is utilized as the solvent during the process of ink slurry preparation. After continuous stirring, the resulting slurry is coated onto a stainless steel circular mesh with a diameter of 12 mm, followed by drying in a vacuum oven at 80 ℃ for 12 h. The active material loading was approximately 2 mg cm^{-2}. The electrochemical analysis of all samples is performed using a CR2032 coin cell with zinc foil as the negative electrode, glass fiber as the separator, and 2 M $ZnSO_4$, 2 M $ZnSO_4$ + 0.2 M $MnSO_4$ or 2 M $ZnSO_4$ + 0.5 M $MnSO_4$ aqueous solution as the electrolyte. Cyclic voltammetry (CV) and electrochemical impedance spectroscopy (EIS) are conducted using CHI660E or PARSTAT MC potentiostats. Unless specified otherwise, all potentials are referenced to Zn/Zn^{2+}. The CV scans are performed within the range of 1-1.85 V at a scan rate of 0.1 mV s^{-1}, while EIS measurements are carried out across a frequency spectrum from 10^5 to 0.01 Hz, with an alternating potential amplitude of 5 mV. A battery test system (LAND MTI-5 V 10 mA) is utilized to assess the cycling and charge–discharge characteristics of the coin cells.

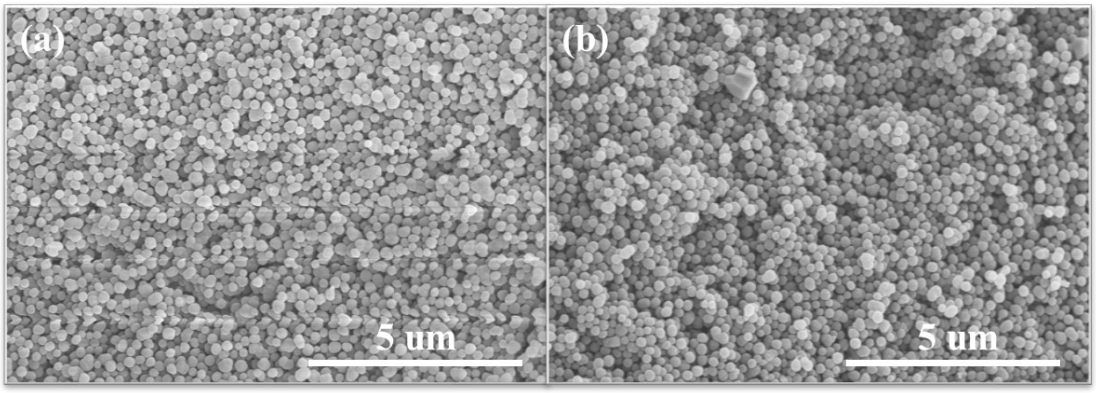

Fig. S1. SEM images of the (a) Mn-PDA and (b) MnO-C/PDA.

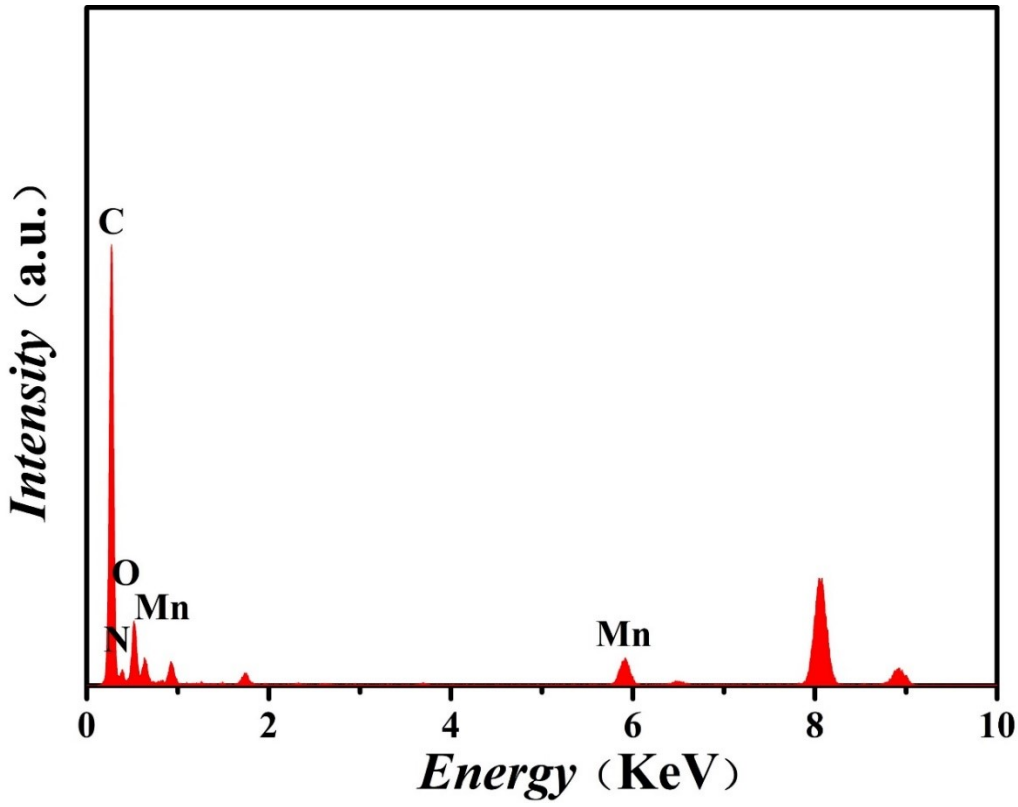

Fig. S2. EDS spectrum of the MnO-C/PDA.

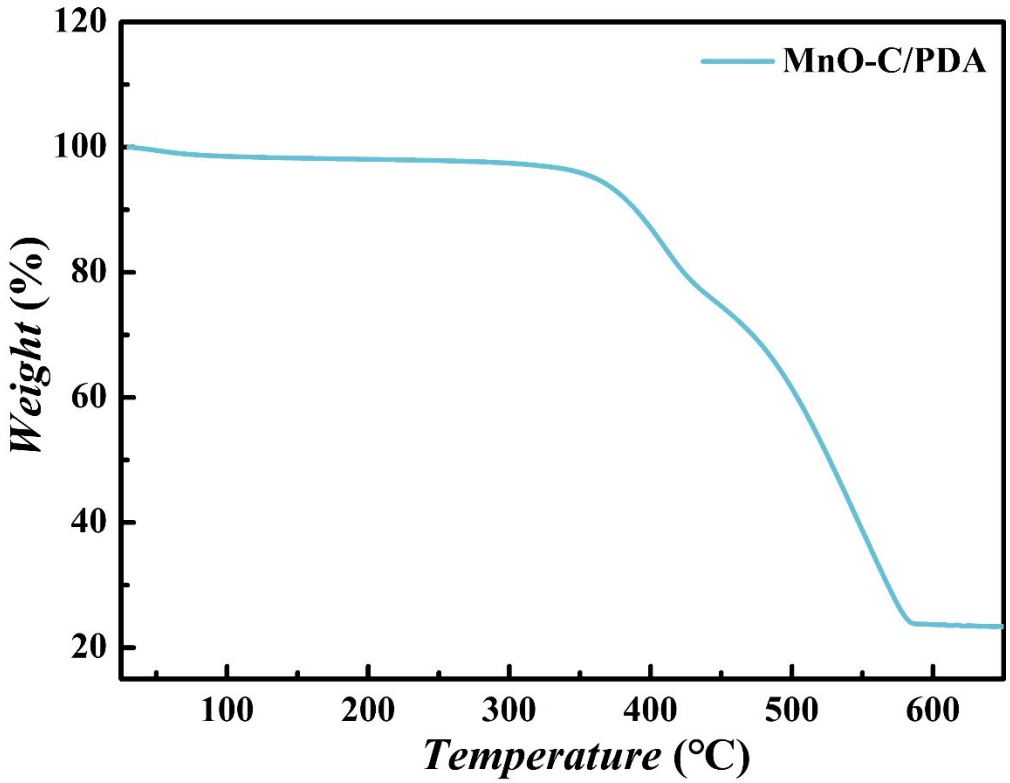

Fig. S3. TGA curve of the MnO-C/PDA.

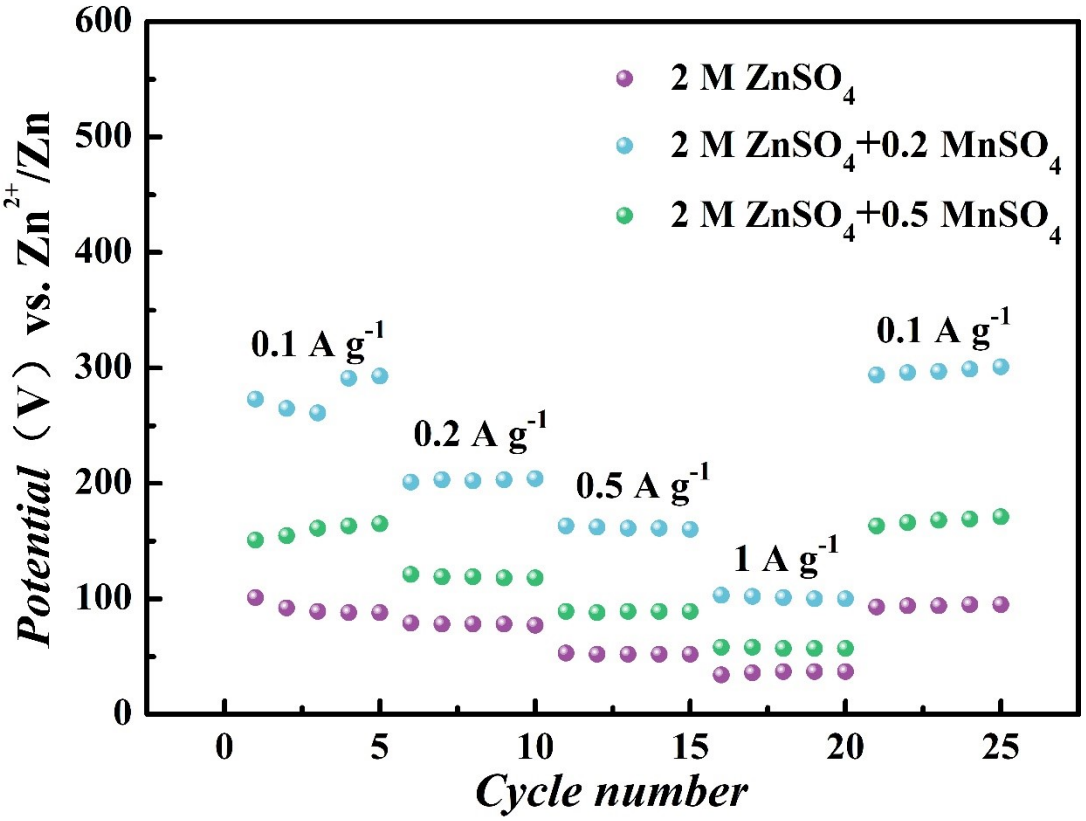

Fig. S4. Rate performances of the MnO-C/PDA in 2 M $ZnSO_4$, 2 M $ZnSO_4$ + 0.2 M $MnSO_4$ and 2 M $ZnSO_4$ + 0.5 M $MnSO_4$ electrolytes.

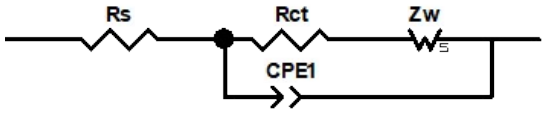

Fig. S5. The fitted equivalent circuit of EIS.

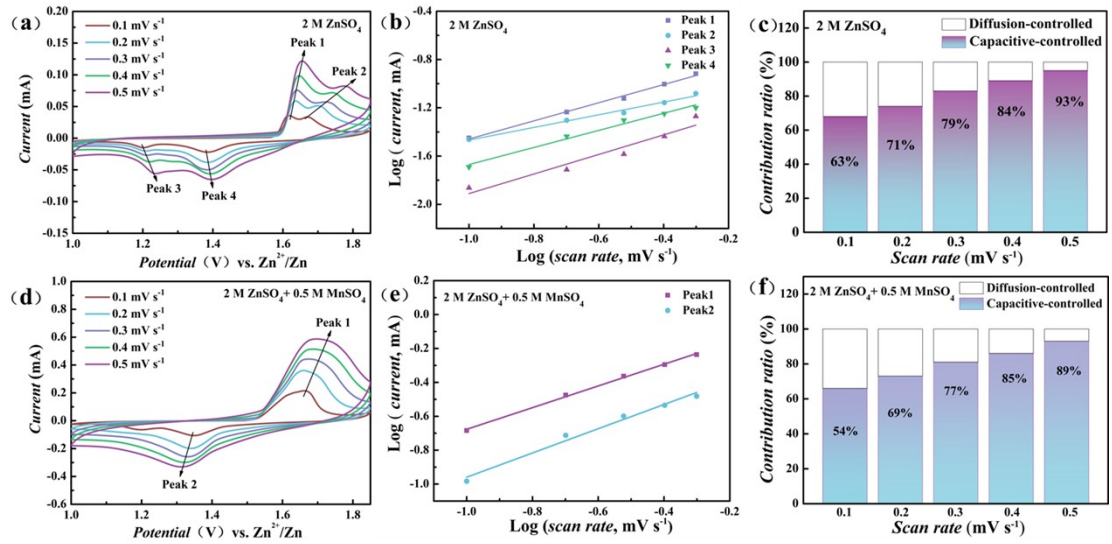

Fig. S6. CV curves of MnO-C/PDA ranging from 0.1 to 0.9 mV s^{-1} in (a) 2 M $ZnSO_4$ and (d) 2 M $ZnSO_4$ + 0.5 M $MnSO_4$ electrolytes; Log (peak current) versus log (scan rate) plot of MnO-C/PDA in (b) 2 M $ZnSO_4$ and (e) 2 M $ZnSO_4$ + 0.5 M $MnSO_4$ electrolytes; Contribution of the capacitive-controlled process to the capacity of MnO-C/PDA in (c) 2 M $ZnSO_4$ and (f) 2 M $ZnSO_4$ + 0.5 M $MnSO_4$ electrolytes.

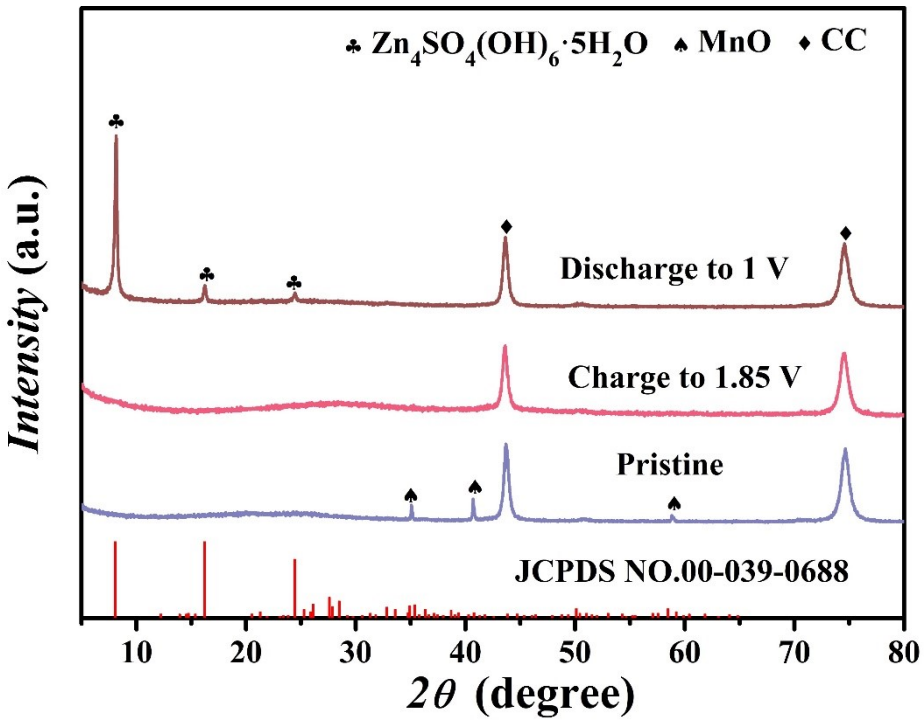

Fig. S7. Ex-situ XRD patterns of MnO-C/PDA in 2 M $ZnSO_4$ electrolyte at the initial, charging and discharging states.

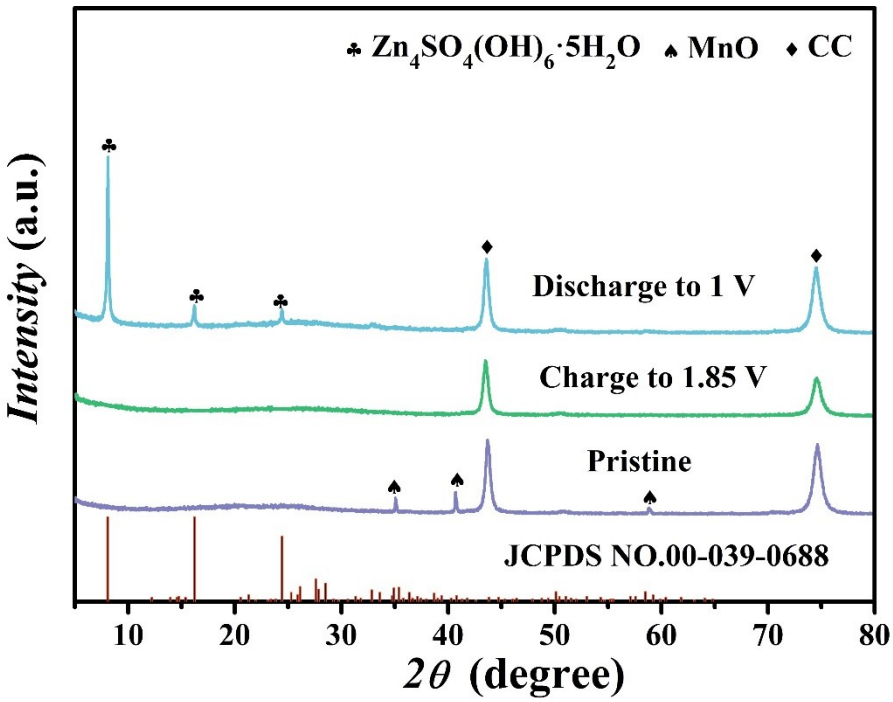

Fig. S8. Ex-situ XRD patterns of MnO-C/PDA in 2 M $ZnSO_4$ + 0.5 M $MnSO_4$ electrolyte at the initial, charging and discharging states.

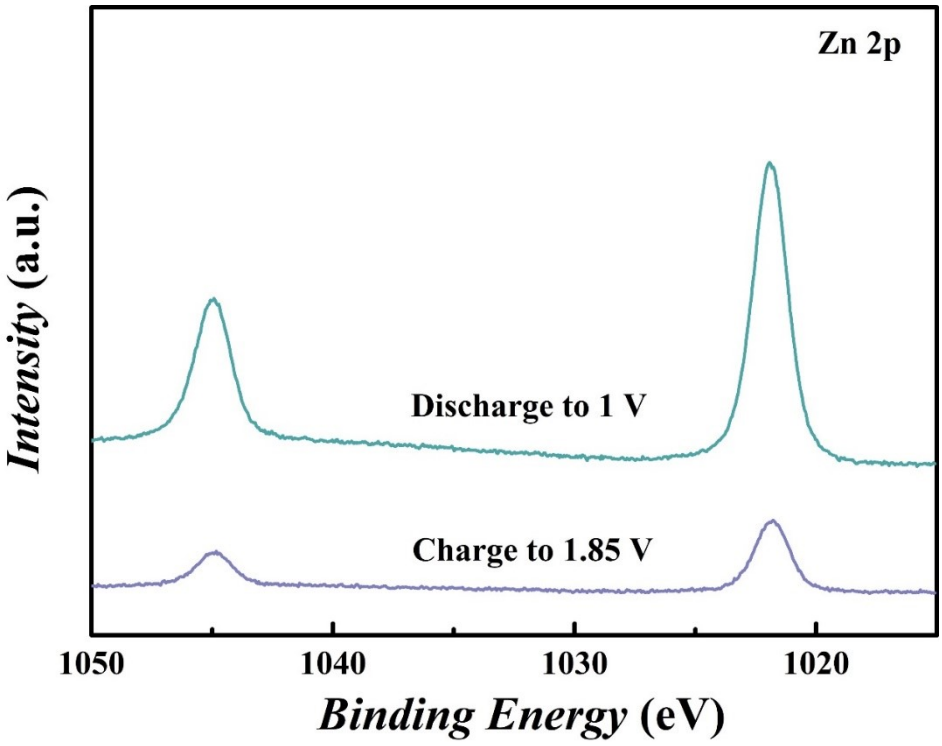

Fig. S9. XPS spectra of Zn 2p region at the charging and discharging states.

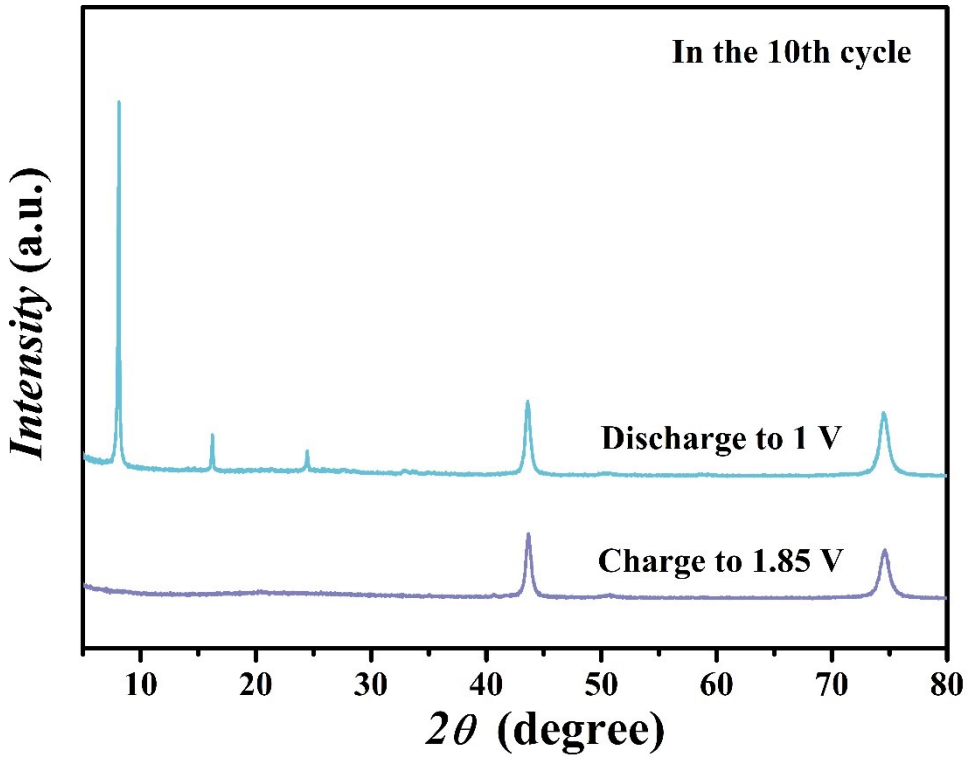

Fig. S10. Ex-situ XRD patterns of MnO-C/PDA in 2 M $ZnSO_4$ + 0.2 M $MnSO_4$ electrolyte for the charging and discharging states at the 10th cycle.

Table S1. Performance comparison of aqueous ZIBs with manganese oxide-based materials as cathodes.

Cathode material	Electrolyte	Specific capacity	Capacity retention	Ref.
MnO-C/PDA	2 M $ZnSO_4$+ 0.2 M $MnSO_4$	295.4 mA h g^{-1} at 0.2 A g^{-1}	88.9% after 500 cycles at 1 A g^{-1}	This work
F-MO	2 M $ZnSO_4$+ 0.2 M $MnSO_4$	288 mA h g^{-1} at 0.1 A g^{-1}	96% after 200 cycles at 0.2 A g^{-1}	1
MnO_2 @MXene	2 M $ZnSO_4$+ 0.2 M $MnSO_4$	184 mA h g^{-1} at 0.05 A g^{-1}	84.5% after 1000 cycles at 0.1 A g^{-1}	2
HCM	2 M $ZnSO_4$+ 0.3 M $MnSO_4$	341 mA h g^{-1} at 0.2 A g^{-1}	87% after 3500 cycles at 2 A g^{-1}	3
ε- MnO_2@N	2 M $ZnSO_4$+ 0.5 M $MnSO_4$	183.4 mA h g^{-1} at 0.5 A g^{-1}	83% after 1000 cycles at 5 A g^{-1}	4
δ- MnO_2	1 M $ZnSO_4$	252 mA h g^{-1} at 0.083 A g^{-1}	43% after 100 cycles at 0.083 A g^{-1}	5
Mn_3O_4/CP	2 M $ZnSO_4$+ 0.2 M $MnSO_4$	201 mA h g^{-1} at 0.3 A g^{-1}	No decreasing after 200 cycles at 1 A g^{-1}	6
$ZnMn_2O_4$/NG	1 M $ZnSO_4$+ 0.05 M $MnSO_4$	232 mA h g^{-1} at 0.1 A g^{-1}	97.4% after 2500 cycles at 1 A g^{-1}	7
O_{cu}-Mn_2O_3	3 M $ZnSO_4$+ 0.1 M $MnSO_4$	241 mA h g^{-1} at 0.1 A g^{-1}	88% after 600 cycles at 1 A g^{-1}	8
ZMO/CNTs	1 M $ZnSO_4$+ 0.1 M $MnSO_4$	220.3 mA h g^{-1} at 0.1 A g^{-1}	97.0% after 2000 cycles at 3 A g^{-1}	9

Mn_3O_4@HCFs	2 M ZnSO4+ 0.15 M MnSO4	215.8 mA h g^{-1} at 0.3 A g^{-1}	No decreasing after 1300 cycles at 0.4 A g^{-1}	[10]
Fe/α-MnO_2@PPy	2 M $ZnSO_4$+ 0.1 M $MnSO_4$	270 mA h g^{-1} at 0.1 A g^{-1}	71.4.% after 100 cycles at 0.1 A g^{-1}	[11]
α-MnO_2/CNT HMs	2 M $ZnSO_4$+ 0.1 M $MnSO_4$	296 mA h g^{-1} at 0.2 A g^{-1}	No decreasing after 100 cycles at 0.2 A g^{-1}	[12]
Ti-MnO_2	3 M $Zn(CF_3SO_3)_2$ + 0.1 M $Mn(CF_3SO_3)_2$	259 mA h g^{-1} at 0.1 A g^{-1}	80% after 4000 cycles at 1 A g^{-1}	[13]

References

1. D. Wang, Z. Liu, X.-W. Gao, Q. Gu, L. Zhao and W.-B. Luo, Massive anionic fluorine substitution two-dimensional δ-MnO_2 nanosheets for high-performance aqueous zinc-ion battery, J. Energy Storage, 2023, **72**, 108740.
2. L. Wu, Y. Mei, Y. Liu, W. Xu, M. Zhang, Y. Dong and Z.-S. Wu, Interfacial synthesis of strongly-coupled δ-MnO_2/MXene heteronanosheets for stable zinc ion batteries with Zn^{2+}-exclusive storage mechanism, Chem. Eng. J., 2023, **459**, 141662.
3. S. Luo, J. Xu, B. Yuan, L. Chen, L. Xu, R. Zheng, Y. Wang, M. Zhang, Y. Lu and Y. Luo, Biomass-derived nitrogen-doped carbon fiber driven δ-MnO_2 for aqueous zinc-ion batteries with high energy and power density, *Carbon*, 2023, **214**, 118334.
4. Y. Zhang, Y. Liu, Z. Liu, X. Wu, Y. Wen, H. Chen, X. Ni, G. Liu, J. Huang and S. Peng, MnO_2 cathode materials with the improved stability via nitrogen doping for aqueous zinc-ion batteries, J. Energy Chem., 2022, **64**, 23-32.
5. M. H. Alfaruqi, J. Gim, S. Kim, J. Song, D. T. Pham, J. Jo, Z. Xiu, V. Mathew and J. Kim, A layered δ-MnO_2 nanoflake cathode with high zinc-storage capacities for eco-friendly battery applications, Electrochem. Commun., 2015, **60**, 121-125.
6. A. Dhiman and D. G. Ivey, Electrodeposited manganese oxide on carbon paper for zinc-ion battery cathodes, *Batteries & Supercaps*, 2020, **3**, 293-305.
7. L. Chen, Z. Yang, H. Qin, X. Zeng and J. Meng, Advanced electrochemical

performance of $ZnMn_2O_4$/N-doped graphene hybrid as cathode material for zinc ion battery, J. Power Sources, 2019, **425**, 162-169.

8. N. Liu, X. Wu, Y. Yin, A. Chen, C. Zhao, Z. Guo, L. Fan and N. Zhang, Constructing the efficient ion diffusion pathway by introducing oxygen defects in Mn_2O_3 for high-performance aqueous zinc-ion batteries, ACS Appl. Mater. Interfaces, 2020, **12**, 28199-28205.

9. F. Gao, B. Mei, X. Xu, J. Ren, D. Zhao, Z. Zhang, Z. Wang, Y. Wu, X. Liu and Y. Zhang, Rational design of $ZnMn_2O_4$ nanoparticles on carbon nanotubes for high-rate and durable aqueous zinc-ion batteries, Chem. Eng. J., 2022, **448**, 137742.

10. J. Long, Z. Yang, F. Yang, J. Cuan and J. Wu, Electrospun core-shell Mn_3O_4/carbon fibers as high-performance cathode materials for aqueous zinc-ion batteries, Electrochim. Acta, 2020, **344**, 136155.

11. J.-W. Xu, Q.-L. Gao, Y.-M. Xia, X.-S. Lin, W.-L. Liu, M.-M. Ren, F.-G. Kong, S.-J. Wang and C. Lin, High-performance reversible aqueous zinc-ion battery based on iron-doped alpha-manganese dioxide coated by polypyrrole, J. Colloid Interface Sci., 2021, **598**, 419-429.

12. Y. Liu, X. Chi, Q. Han, Y. Du, J. Huang, Y. Liu and J. Yang, α-MnO_2 nanofibers/carbon nanotubes hierarchically assembled microspheres: Approaching practical applications of high-performance aqueous Zn-ion batteries, J. Power Sources, 2019, **443**, 227244.

13. S. Lian, C. Sun, W. Xu, W. Huo, Y. Luo, K. Zhao, G. Yao, W. Xu, Y. Zhang and

Z. Li, Built-in oriented electric field facilitating durable $ZnMnO_2$ battery, *Nano Energy*, 2019, **62**, 79-84.